Computer Vision and Image Understanding **84,** 1–29 (2001)
doi:10.1006/cviu.2001.0950

Color Models for Outdoor Machine Vision

Shashi D. Buluswar

Department of Computer Science, Northwestern University, Evanston, Illinois 60208

and

Bruce A. Draper

Department of Computer Science, Colorado State University, Ft. Collins, Colorado 80523

Received May 19, 2000; accepted November 20, 2001; published online

This study develops models for illumination and surface reflectance for use in outdoor color vision, and in particular for predicting the color of surfaces under outdoor conditions. Existing daylight and reflectance models have limitations that reduce their applicability in outdoor contexts. This work makes three specific contributions: (i) an explanation of why the current standard CIE daylight model cannot be used to predict the color of light incident on outdoor surfaces, (ii) a model (table) of the measured color of daylight for a broad range of sky conditions, and (iii) a simplified adaptation of the dichromatic reflectance model for use with the developed daylight model. A series of experiments measure the accuracy of the daylight and reflectance models, and their applicability to outdoor color vision applications, by predicting the colors of surfaces in real images.

Key Words: color; daylight; outdoor images; reflectance model; photometric function.

1. INTRODUCTION

Many outdoor machine vision applications, most notably color-based recognition, rely heavily on the accurate modeling of daylight and surface reflectance. Unfortunately—as Section 3 will show—the existing standard CIE daylight model [29] has drawbacks that limit its applicability to predict the color of incident light; similarly, as Section 4 will show, existing surface reflectance models [37, 45, 50] are not easily applied to outdoor images. In that context, this study makes three contributions: (i) an explanation of why the CIE daylight model cannot be used to predict light incident upon surfaces in machine vision images, (ii) a model of daylight color (in the form of a table) showing the measured color of

1077-3142/01 $35.00

4-Color Artwork

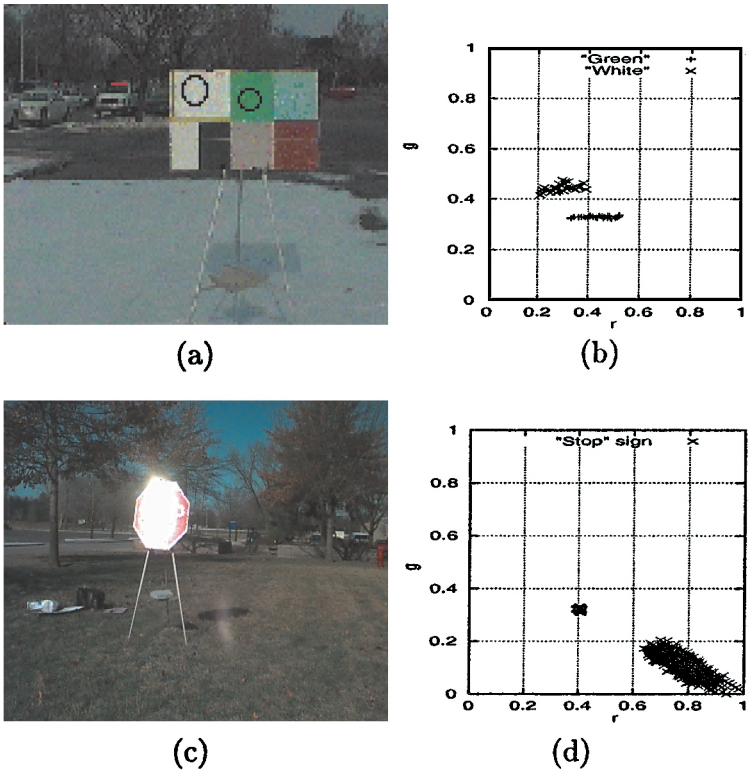

FIG. 1. Variation in the measured color of two types of surfaces—matte and specular—taken under varying daylight conditions and illumination/viewing angles: (a) sample matte surfaces and (c) a sample specular surface (shown here facing the sun). Measured rgb values for these surfaces across many images are shown in (b) and (d). To get reliable color data, the values in (b) were averaged across the pixels in the circles shown in (a), while the values in (d) are averages across the sign surface in (c).

daylight for a broad range of sky conditions, and (iii) an adaptation of the frequently used dichromatic reflectance model [50], which can be used with the daylight model. Finally, experiments test the applicability of the models to color-based recognition by predicting the colors of surfaces in real outdoor images.

To demonstrate why accurate models of daylight and reflectance are important for outdoor machine vision, Fig. 1 shows how the measured color of surfaces can vary due to changes in daylight and surface orientation. Figure 1a shows matte surfaces—white and green paper, and Fig. 1c shows a specular traffic ("Stop") sign.[1] The samples were measured over 50 images of each surface, under a variety of sky conditions ranging from a clear sky to an overcast sky, with the sun angle (elevation) between 5° (dawn and dusk) and 60° (mid-day). The illumination angle (i.e., the orientation in azimuth of the surface normal with respect to the sun) varied from 0° to 180°, and the viewing angle (the angle in azimuth between the optical axis and the surface) varied from 0° to 90°. The measured color of the surfaces was determined by averaging the pixels over a small region in each image to reduce the effect

[1] Note that the traffic signs used in this study are privately owned and do not have the retroreflective or fluorescent properties sometimes required for public signs.

of pixel-level noise. Figures 1c and 1d show the measured color of the surface patches over the 50 images in rgb color space.[2]

What is notable about the matte examples is that the measured samples for each surface vary by as much as 0.2 units in rgb, on a scale of 0–1; this represents about 105% of the distance between the surface colors in rgb. In other words, the overall variation in the measured color of a single surface can be greater than the difference between two perceptually distinct colors (in this case, white and green). Figure 1c shows an image of a "Stop" sign facing the sun; Fig. 1d shows the variation of the measured color rgb. The samples demonstrate that specular surfaces create bimodal distributions of measured colors because of the differences between the specular and diffuse (Lambertian) reflections. In addition, Fig. 1c shows that as viewing angle changes, a surface can exhibit both specular and nonspecular reflections in a single image.

While these observations are not new, they demonstrate that measured color is a function of context, particularly illumination, reflectance, and orientation. The implication is that inaccurate modeling of these factors can lead to gross errors in predicted colors. The goal of this work is to build practical models of daylight and reflectance to predict the measured colors of surfaces. To that end, a model of daylight is developed that predicts the color of incident daylight from the sun angle and cloud cover. This model attempts to address disadvantages of the standard CIE daylight model [29] by mapping from context to color and by accounting for the wide field-of-view typical of surfaces in outdoor settings (details in Section 3). Then, existing surface reflectance models are simplified for use in normalized color space under an extended light source (daylight); this makes it easier to apply hybrid (i.e., specular + diffuse) models in outdoor contexts. Finally, a series of experiments tests the effectiveness of the two models in predicting the color of target surfaces in real outdoor images.

2. COLOR CONSTANCY

Research in color machine vision has a rich history, although relatively little of it explores issues in outdoor imagery. This work builds directly on the CIE model of daylight and on previous physics-based models of surface reflectance; see Sections 3 and 4, respectively. In addition, there has been research on color vision with respect to parametric classification [7], machine learning techniques [4, 9], color-based segmentation [35, 42, 49], application-driven approaches [7, 46], and color indexing [18, 52].

Another line of research has been work on the so-called *color constancy problem*. Whereas this paper predicts color by deriving models for illumination and reflectance in outdoor imagery, color constancy algorithms match similarly colored surfaces under unknown illumination without a-priori knowledge of the surface reflectance functions. Since one motivation for predicting color is to match surfaces, color constancy can be thought of as an alternate approach to a similar problem. We therefore briefly review color constancy algorithms; readers who are uninterested in or are already familiar with this material may choose to skip to Section 3.

[2] rgb space is a normalized form of RGB and is used to eliminate the effect of brightness. As Section 3 will show, rgb color is easier to model under outdoor conditions than RGB. In rgb, $r = R/(R+G+B)$, $g = G/(R+G+B)$, and $b = B/(R+G+B)$; hence, $r+g+b = 1$. Given r and g, $b = 1-r-g$. Therefore, rgb is a two-dimensional space that can be represented by an rg plane. Note also that while there are canonical RGB spaces, each camera should be calibrated to determine its response parameters. The calibration parameters for the camera used in this study are shown in Table 2 in Appendix A.

Depending on their assumptions and techniques, color constancy algorithms can be classified into six categories [16]: (1) those which make assumptions about the statistical distribution of surface colors in the scene, (2) those which make assumptions about the reflection and illumination spectral basis functions, (3) those assuming a fixed illuminant and surface gamut, (4) those which obtain an indirect measure of the illuminant, (5) those which require multiple illuminants, and (6) those which require the presence of surfaces of known reflectance in the scene. Among the algorithms that make assumptions about statistical distributions, von Kries and Buchsbaum assume that the average surface reflectance over the entire scene is gray (the gray-world assumption) [2, 31]; Gershon *et al*. [21] assume that the average scene reflectance matches that of some other known color; Vrhel and Trussell [53] assume knowledge of the general covariance structure of the illuminant, given a small set of illuminants; and Freeman and Brainard [15] assume that the illumination and reflection follow known probability distributions. These methods are effective when their assumptions are valid. Unfortunately, as Fig. 1 shows, no general assumptions can be made about the distribution of surface colors without knowledge of the reflectance, even if the distribution of daylight color is known. Consequently, these methods are too restrictive for all but very constrained scenes.

The second category of color constancy algorithms makes assumptions about the dimensionality of spectral basis functions [51] required to accurately model illumination and surface reflectance. For instance, Maloney and Wandell [34] and Yuille [54] assume that the linear combination of two basis functions is sufficient. It is not clear how such assumptions about the dimensionality of spectral basis functions in wavelength space apply to a reduced-dimension color space, such as the tristimulus *RGB* (Finlayson *et al*. [12] discuss this issue in greater detail).

Among the algorithms that make assumptions about image gamuts is Forsyth's CRULE algorithm [14], which maps the gamut of possible image colors to another gamut of colors that is known a-priori, so that the number of possible mappings restricts the set of possible illuminants. In a variation of CRULE, Finlayson [10] applies a spectral sharpening transform to the sensory data to relax the gamut constraints. This method can be applied to algorithms using linear basis functions [34, 54] as well. CRULE represents a significant advance in color constancy, but its assumptions about gamut mapping restrict it to matte Mondrian surfaces under controlled illumination. Ohta and Hayashi [41] assume a known gamut of illuminants (indoor lighting following the CIE model) and use multi-image correspondence to determine the specific illuminant from the known set. By restricting the illumination, this method can only be applied to synthetic or highly constrained indoor images.

Another class of algorithms uses indirect measures of illumination. For instance, Shafer [50] and Klinker *et al*. [30] use surface specularities (Sato and Ikeuchi [48] use a similar principle, but not for color constancy), and Funt and Drew [17] use interreflections to measure the illuminant. These methods assume a single point-source illuminant, which limits their application in outdoor contexts, since sunlight/daylight is a composite, extended light source.

In yet another approach, D'Zmura and Iverson [55] and Finlayson *et al*. [11] assume multiple illuminants incident upon multiple instances of a single surface. The problem with these approaches is that they require identification of the same surface in two spatially distinct parts of the image that are subject to different illuminants. Once again, the approaches have been shown to be effective only on Mondrian or similarly restricted images. In a variation of this approach, Finlayson *et al*. [13] show good results on a set of synthetic and real

images by correlating image colors with the colors that can occur under each set of possible illuminants.

The final group of algorithms assumes the presence of surfaces of known reflectance in the scene and then determines the illuminant. For instance, Land's Retinex algorithm [32] and its many variations rely, for accurate estimation, on the presence of a surface of maximal (white) reflectance within the scene. Similarly, Novak and Shafer's supervised color constancy algorithm [40] requires surfaces of other known reflectances.

Others [4, 20] have approached color constancy as a machine learning problem with strong results. One potential issue with such approaches is that the training images need to represent the gamut of possible conditions that can occur; in real outdoor images, such training data may not be available.

Funt and Finlayson [16, 19] discuss various approaches to color constancy in greater detail. As that and the above discussion show, the assumptions made by most of the aforementioned algorithms limit their application to restricted images under constrained lighting; certainly, few such methods have been applied to relatively unconstrained outdoor imagery. It therefore makes sense to develop models for outdoor illumination and surface reflectance under outdoor conditions.

3. A MODEL OF DAYLIGHT COLOR

3.1. The CIE Daylight Model

The standard model of daylight is the CIE daylight model [29], based on 622 radiometric measurements of daylight collected separately over several months in the U.S., Canada, and England [3, 6, 23]. The radiometric measurements were made by aiming a narrow tube [6] with a very small field-of-view (e.g., 0.5° and 1.5° [43]) at selected portions of the sky. The light going through the collection tube falls on a planar surface covered with barium sulphate (or a similar "white" material), and the spectral power distribution of the surface is recorded. Careful precautions were taken to eliminate the effect of stray light; the data was collected on rooftops, where the rooftop, nearby walls, and even the collection tube were covered by black light-absorbent material [6].

The CIE's parametric model was obtained by mapping the spectral power distributions of each of the 622 samples into the CIE chromaticity space and fitting a parabola to the points. In particular, the CIE model predicts that the color of daylight is

$$y = 2.87x - 3.0x^2 - 0.275, \tag{1}$$

where $0.25 \leq x \leq 0.38$. In rgb space (which is a linear transform of the chromaticity space [25]), the model is

$$g = 0.866r - 0.831r^2 + 0.134, \tag{2}$$

where $0.19 \leq r \leq 0.51$. Figure 2 plots the CIE daylight model in rgb; the figure also plots the CIE model in the color circle. The regions of the function representing (approximately) sunlight and skylight (Fig. 2b) have been determined empirically, based on radiometric measurements made by Condit and Grum [6] and the measurements shown in Table 1 (which is discussed later in this section).

TABLE 1

Daylight Color Indexed by Sun Angle, Cloud Cover, and Sun Visibility (SV): Facing the Sun (rgb_{sn}), and Facing Away (rgb_a); Brightness (V), Number of Samples and Standard Deviation (SD) are also Shown, Along with the Average Color (rgb_{sk}) of the Sky

Sun ∠	Cld %	SV	rgb_{sn}	SD	V_{sn}	SD	rgb_a	SD	V_a	SD	#	rgb_{sk}
0–5	0–20	1	0.436	0.006	195	24	0.288	0.009	53	29	8	0.260
			0.349				0.302					0.299
0–5	20–50	1	0.436	0.006	186	31	0.296	0.012	48	33	9	0.277
			0.349				0.312					0.302
0–5	50–70	0.5	0.406	0.008	158	36	0.319	0.009	56	38	11	0.349
			0.344				0.315					0.331
0–5	70–100	0	0.352	0.005	41	22	0.352	0.008	41	26	10	0.355
			0.335				0.335					0.336
6–15	0–20	1	0.394	0.008	206	31	0.288	0.010	58	34	6	0.274
			0.330				0.302					0.305
6–15	20–50	1	0.394	0.009	198	38	0.296	0.009	41	40	6	0.296
			0.340				0.312					0.314
6–15	50–70	0.5	0.368	0.010	167	29	0.319	0.012	41	32	7	0.331
			0.334				0.315					0.330
6–15	70–100	0	0.352	0.008	44	21	0.352	0.007	36	24	6	0.352
			0.335				0.335					0.338
16–25	0–20	1	0.385	0.008	221	28	0.323	0.008	51	34	11	0.301
			0.337				0.334					0.313
16–25	20–50	1	0.385	0.007	215	26	0.323	0.013	51	26	7	0.334
			0.337				0.334					0.323
16–25	50–70	0.5	0.376	0.011	188	30	0.326	0.012	58	32	4	0.337
			0.337				0.336					0.329
16–25	70–100	0	0.352	0.008	50	21	0.352	0.009	48	25	4	0.357
			0.335				0.335					0.335
26–50	0–20	1	0.370	0.008	224	33	0.323	0.009	56	35	9	0.309
			0.332				0.334					0.328
26–50	20–50	1	0.370	0.007	220	29	0.323	0.011	69	35	8	0.333
			0.332				0.334					0.332
26–50	50–70	0.5	0.359	0.006	176	28	0.326	0.010	51	31	4	0.347
			0.337				0.336					0.334
26–50	70–100	0	0.352	0.008	64	24	0.352	0.008	68	29	9	0.354
			0.335				0.335					0.336
51–70	0–20	1	0.350	0.007	249	36	0.323	0.010	71	38	3	0.312
			0.335				0.334					0.330
51–70	20–50	1	0.350	0.009	249	35	0.323	0.013	60	37	5	0.333
			0.335				0.334					0.332
51–70	50–70	0.5	0.359	0.010	170	37	0.326	0.010	43	37	9	0.341
			0.332				0.336					0.332
51–70	70–100	0	0.352	0.008	52	22	0.352	0.008	51	25	8	0.352
			0.335				0.335					0.335

For mathematical simplicity, the discussions in Section 3.3 and thereafter will approximate the CIE parabola by the straight line, also shown in Fig. 2c,

$$g = 0.227 + 0.284r, \tag{3}$$

4-Color Artwork

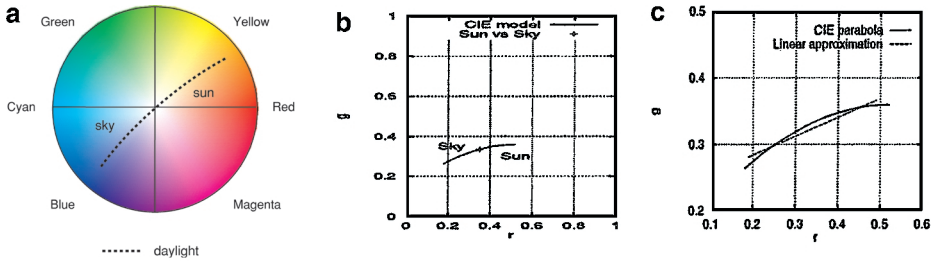

FIG. 2. The CIE parametric model of daylight in (a) the color circle and (b) the rgb space. The sunlight and skylight components have been empirically determined to be on either side of the white point ([0.33, 0.33] in rgb and the center of the color circle). Figure 2c shows a linear approximation to the CIE parabola used in later sections.

determined by fitting a line to points along the locus of the CIE parabola (with an RMS error of about 0.007). Figure 2c compares the linear and quadratic models.

3.2. A Model of Daylight Indexed by Context

While the CIE model predicts the range of possible colors of daylight, it is not indexed by context. As a result, it does not predict the color of daylight in particular images. One contribution of this work is to present a model of daylight indexed by scene context. To develop this model, we collected samples of daylight from 224 color images of a calibrated matte white surface (Munsell number $N9/$), knowing that the measured color of a white surface is the color of the light incident upon it. The images were selected to sample as many sun angles (from sunrise/sunset to high noon) and weather conditions (from sunny to completely overcast) as possible. To reduce the effect of pixel-level noise, the color of the white surface was sampled as the average of a 20 pixel $\times$ 20-pixel area. Figure 3 shows the sampling apparatus, along with samples of the color of daylight obtained from the set of 224 images, plotted in rgb.

As Fig. 3a shows, the white board was mounted on a tripod alongside matte surfaces of different colors. The tripod had angular markings at every 5° on a rotatable head mount. During data collection, the angular markings on the tripod were used to vary the azimuth of

4-Color Artwork

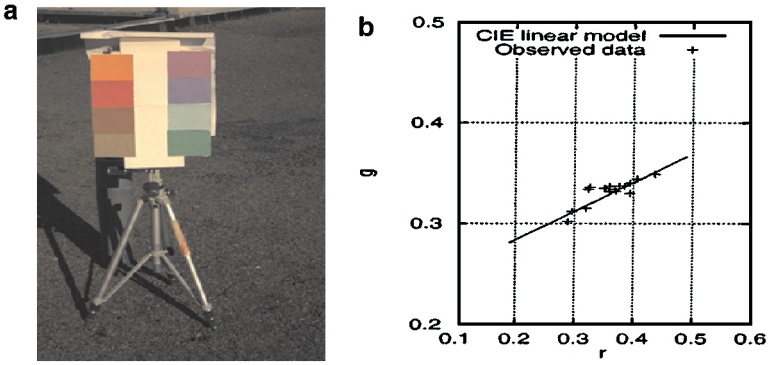

FIG. 3. Samples of daylight color obtained from color images, compared to the CIE model. The white surface in the center of image in Fig. 3a reflects the color of the incident light. These samples are plotted along with the linear approximation of the CIE model in Fig. 3b.

the viewing geometry, with images taken every 10°. The viewing geometry with respect to pitch was (approximately) fixed by maintaining a constant distance between the camera and the surface, as well as a constant camera height. For the measurements at each sampled sun angle, the illumination geometry was also fixed with respect to pitch, but varied in azimuth. Using this procedure, it was determined that for almost[3] the whole 180° range, where the sun is directly shining on the surface, the color of the incident daylight does not change with respect to relative viewing geometry. Similarly, as long as the surface is facing away from the sun, the color of the incident light is that of the ambient skylight. As a result, the viewing geometry context in our daylight model is a single binary term: a surface is either facing the sun or not.

Table 1 presents our daylight model as a table mapping imaging conditions onto the color of incident daylight. In particular, since the color of daylight depends primarily on sun angle, sun visibility, cloud cover, and surface orientation (relative to the sun), Table 1 is indexed by these factors. The sun angle is the vertical rise of the sun and can be calculated from a standard astronomical equation, given the location (latitude and longitude) and time/date [36]. For experimental purposes, the sun angle was calculated using this technique and then confirmed through physical measurement with a protractor. The cloud cover is an approximate measure of the percentage of the sky covered by clouds. The sun visibility factor is an approximate measure of the clarity of the sun, scaled from 0 to 1.[4] For instance, if the sun is completely covered by a dark cloud, the visibility factor is 0, while if the sun is unobscured, the factor is 1. If the sun is behind a thin cloud but still perceptible, the factor may be about 0.5.

For each of these conditions, Table 1 lists the average normalized rgb color and brightness (intensity) of daylight in two directions: facing the sun (rgb_{sn} and V_{sn}), and away from the sun (rgb_a and V_a).[5] The standard deviations of these measurements are also shown, along with the number of data samples used to derive them. Note that the standard deviations of the brightness values are too high to accurately predict the brightness of daylight under a given set of conditions. Finally, the last column of Table 1 gives the average sky color (rgb_{sk}) as reflected off a Munsell white surface that is facing up toward the sky, rather than a vertically oriented white surface (see Section 3.3).

The data in Table 1 was collected at three locations in the U.S.—rural Massachusetts, suburban Detroit, and suburban Chicago—in 1995, 1996, and 1997, respectively. Each year, at each location, the data was collected over six months: September through February. Hence, this data does not account for possible variations due to seasonal factors (such as summer haze, etc.). In addition, the effect of smog is uncertain, and the applicability of the model to areas with significantly different levels of smog or haze is not clear [24].

3.3. Disadvantages of the CIE Model

Although the CIE model of daylight is not indexed by context, it is based on a sound physical theory (blackbody radiation) and careful radiometric measurements. It is therefore

[3] At the extreme viewing angles (e.g., near the −90° and 90° viewing angles), too little of the surface is visible for any meaningful analysis.

[4] The sun visibility factor affects the nature of the incident light in two ways: (1) it affects the color of the incident sunlight as discussed here, and (2) it affects specular reflectance as discussed in Section 4.

[5] The measurement of brightness values in digital cameras depends on the gain setting. For the data in these samples, the CCD gain was fixed at 2.0 e-/count. Details of the effect of the gain control can be found in camera users' manuals or other reference books [28].

prudent to compare the predictions from Table 1 with the CIE model. The root-mean-squared error[6] between the linearized CIE model and the observed data is 0.006. Thus the colors predicted by Table 1 are reasonably consistent with the CIE's model of daylight. However, despite sampling all the conditions in Table 1 (including sunset, sunrise, etc.), we observed a much smaller range of daylight colors than that predicted by the CIE model. In particular, the CIE model predicts daylight colors ranging approximately from $r = 0.19$, $g = 0.27$ (measured in rgb space) to $r = 0.51$, $g = 0.36$; the values in Table 1 range only from $r = 0.29$, $g = 0.30$ to $r = 0.44$, $g = 0.35$. Thus the data in Table 1 accounts for only about 46% of the CIE daylight curve.

This discrepancy between the two models is instructive in that it results from the different sampling methods used. In particular, most of the discrepancy in the range of daylight colors is a field-of-view effect: the CIE studies measured the color of the sky through a narrow collection tube, while we measured it as the light reflected off a planar surface. Since the surface is exposed to light from as much as half the sky, our measurements effectively average light from across large portions of the sky, while the CIE study pinpoints specific locations in the sky. The rest of the difference can be explained by light reflecting off the ground: the CIE took their measurements on blackened rooftops, whereas we took ours at a fixed height over neutral colored but nonetheless reflective ground. As a result, the CIE model is a better predictor of sky colors, whereas our data is a better model of the light incident on surfaces in outdoor images.

3.3.1. The Field-of-View Effect

As Table 1 suggests, daylight colors can be divided into two groups. Those with r values of greater than 0.33 are "reddish" and correspond to direct sunlight; those with r values below 0.33 are "bluish" and correspond to ambient skylight. If we only consider skylight samples, we find that our data stretches from [0.288, 0.302] to [0.326, 0.336], a distance of 0.051 in normalized rgb. On the other hand, the raw CIE data stretches from [0.180, 0.264] to [0.320, 0.326], a spread of 0.146. Since the spread is representative of the extent of variation in color, the data indicates that the variation in ambient skylight according to our samples is only 35% of the variation predicted by the CIE model. Perceptually, this means that the color of skylight can be significantly "bluer" in the CIE model than in our observations. This happens in spite of the fact that the documented illuminating conditions [6] from the CIE studies were also included in our study.[7]

Since there is no documentation on the specific set of conditions that resulted in particular samples in the CIE data, a comparable radiometric study [43] is used. That study recorded an rgb value of [0.180, 0.303] from a "cloudless sky at sunset" [43], from a portion of the sky in the opposite direction from the sun. For the same set of conditions, our data recorded an rgb value of [0.288, 0.302]. This discrepancy constitutes a shift of 0.108.

In addition to a clear sky with a setting sun, the color of the incident light from a direction away from the sun was sampled for two other conditions: a clear sky with the sun at 30° and an overcast sky. For the clear sky, our data showed a value of [0.324, 0.334], whereas the CIE data [6] shows a value of [0.258, 0.313]; this corresponds to a shift of 0.069. On

[6] For every observed value of r (all of which were within the range of the CIE model), a g value was calculated using the CIE model in Eq. (2) and compared to the g value in the observed data.

[7] Of all 622 CIE samples, the specific illumination conditions have been published for only 56 samples from Condit and Grum's study [6].

the other hand, for the overcast sky, our measure was [0.357, 0.335], very close to the CIE measure of [0.360, 0.336].

We hypothesize that most of this difference is a field-of-view effect. The field-of-view of the measuring devices in the radiometric studies was significantly smaller than that of a flat surface. For instance, in Parkkinen's radiometric study the field-of-view of the sampling device was 0.5° (horizontal) and 1.5° (vertical); on the other hand, the white sampling surface used in our apparatus has a field-of-view of nearly 180°. The sampling surface is Lambertian, which means that its color will be affected by light from every source in its field-of-view. As a consequence, while the radiometric equipment measures the color of light from a very small portion of the sky, our apparatus (which is far more representative of surfaces in images) measures the color of incident light from a large portion of the sky—up to half.

To test this hypothesis, we pointed our camera upward and took five direct images of the sky, averaging the pixels in 10×10 image windows (see Appendix A for camera field-of-view information) at various positions in the sky. Figure 4a shows the color of sky pixels. The eastern portion of a clear sky was sampled, with the sun setting in the west—the same conditions as in the radiometric study [43]. The colors at different heights in the sky were [0.201, 0.253] at 5°, [0.188, 0.264] at 15°, [0.254, 0.288] at 30°, [0.261, 0.297] at 45°, and [0.259, 0.298] at 85°. Perceptually, the color of the sky was "bluest" at an elevation of 15° and less "blue" at lower and higher elevations. In addition, the sky was least "blue"

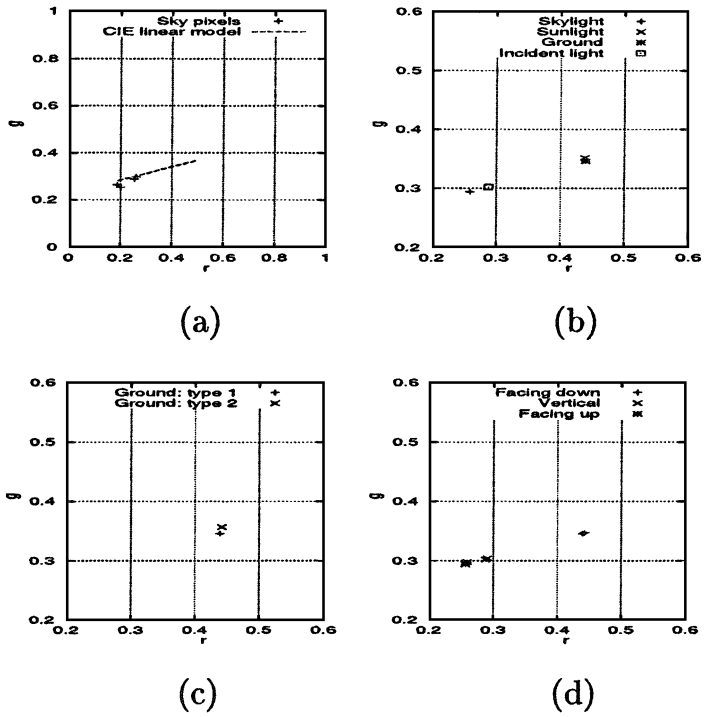

FIG. 4. Samples of daylight color obtained from color images: Figure 4a shows direct samples of the sky at different (elevation) angles; Fig. 4b shows the color of skylight, sunlight, and the effective incident light, measured using the white surface, along with a direct measurement of the "average" ground color; Fig. 4c shows direct samples of the "average" ground color (averaged over 30×30 regions), measured from two different locations; Fig. 4d shows samples of the white surface at different orientations.

across the wide expanse from 45° to 85°, which is the middle portion of the sky. In another image, the white surface was sampled facing the sky (i.e., not vertical as shown in Fig. 3, but almost horizontal). Since the surface is Lambertian, its color is a mixture of the light incident from all directions. The horizontal samples were taken on three different days under the aforementioned conditions. Each time, the rgb value of the surface was about [0.260, 0.299]. This implies that when surfaces face the sky (with no direct sunlight incident upon them), the color of the incident light is dominated by the middle portion of the sky. Hence, it can be assumed that the "average" color of the eastern half of the sky (under a setting sun with no clouds) is [0.260, 0.299]. If this average is accepted as a better representation of the color of skylight than a sample from a small portion of the sky, the color of skylight shifts along the CIE linear function by 0.08 (which is the distance between [0.260, 0.299] and [0.180, 0.303]. Thus, field-of-view effects account for about 74% of the total discrepancy between our model of daylight (given by Table 1) and the CIE model [43].

For a clear sky with the sun at 30°, the color of the incident light (with the surface standing vertically) was [0.324, 0.334], while the CIE measurement for the same conditions is [0.258, 0.313]. Hence, the discrepancy was a shift of 0.069. Direct measurements of the sky color (using averages from 10×10-image windows) were [0.282, 0.303] at 5°, [0.256, 0.314] at 15°, [0.308, 0.326] at 30°, [0.311, 0.329] at 45°, and [0.310, 0.328] at 85°. The average color of the sky, as measured by the white surface facing up toward the sky (with no incident sunlight) was [0.309, 0.328]. The distance between the average color of the skylight and the CIE sample was 0.053. All three points lie on (or within two standard deviations of) the CIE linear function, meaning, that the ambient light accounts for about 77% of the discrepancy between the CIE model and ours.

For an overcast sky, the color of the incident light (measured using the vertical sample) was [0.357, 0.335], very close the CIE measure of [0.360, 0.336]. This is because the color across the sky was uniform—the direct measurements were [0.358, 0.336] at 5°, [0.354, 0.334] at 15°, [0.358, 0.335] at 30°, [0.355, 0.336] at 45°, and [0.357, 0.335] at 85°. The average color of the sky (from a surface facing the sky) was [0.357, 0.335], which was, again, the color of the middle portion of the sky. The CIE estimate [6] was [0.360, 0.336], which is very similar to the average color of the sky. This is not surprising since there is very little variation across different portions of an overcast sky. In effect, the exception proves the rule: there is no discrepancy when the sky is uniformly colored, so it must be the variance in color across the sky that creates the discrepancy. Table 1 lists the color of the incident light in the direction of the sun and away from the sun for a number of conditions. The color of the ambient skylight is listed for each of the conditions, and whenever the sky color is not overcast (i.e., when the sky is not uniformly colored), the ambient light accounts for about 75% of the discrepancy between the CIE data and ours.

3.3.2. Ground Reflection

While ambient skylight accounts for about 75% of the discrepancy between the radiometric studies and ours, another 20% is explained by the effect of reflectance off the ground. In our apparatus the white sampling surface is vertical, so it is exposed to light reflected from other objects in the scene as well as from the sky. Of the scene objects, the one that is consistently the largest and closest to the sampling surface is the ground. Since the sampling surface is Lambertian, its measured color will be a combination of light from all sources—in this case, the sky and the ground.

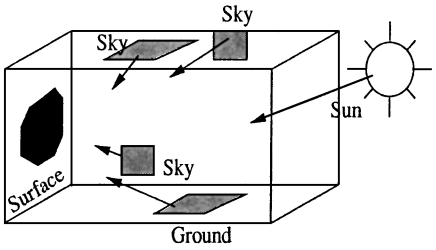

FIG. 5. Six-sided polyhedral model showing light incident upon the surface from five directions: sunlight from one direction, ground reflection the bottom, and skylight from above and the sides.

Figure 4b shows four points:

1. The first sample represents the average color of the sky (as measured by the surface oriented horizontally);
2. The second sample shows the color of the incident sunlight from the direction of the sun (as measured by the surface facing the sun).
3. The third sample shows the color of two types of concrete on which the apparatus rests. The color of these samples is very similar to that of the incident sunlight, which is not surprising since the concrete is gray and is illuminated by sunlight (which, as the reader may recall from Section 3, dominates any ambient skylight).
4. Finally, the fourth sample shows the color of the white surface oriented vertically. This sample represents the color of the effective incident light and lies on the line connecting the two previous points.

The data suggests that the color of the light incident upon a vertical surface facing away from the sun is a combination of the average skylight and the indirect sunlight reflected off the ground. To account for the shift along the CIE linear function due to ground reflection, the three-dimensional world is modeled as a six-sided polyhedral box (see Fig. 5). In this (admittedly crude) model, the white surface faces one side, with its back to another. When the surface faces away from the sun, the side of the box that is behind the surface represents the portion of the sky with the sun. Hence, light is incident upon the surface from five of the six sides. Of these five sides, four represent the sky and one represents the ground. The linear shift is modeled as a weighted sum of the *brightness* of each side. The brightness of the ground depends on its own reflectivity, the brightness of the sunlight and the visibility of the sun (due to cloud cover, etc.). If the average brightness of the ground is represented by g, the ratio of ground brightness to sky brightness is represented by G, and the sun visibility factor is represened by SV, then the effect of ground reflection can be determined from the expression $(4 \times G \times g + g \times SV)$, which represents the distance between the average color of the sky and the color of the ground reflection.

In the samples described in Fig. 4 (i.e., with the setting sun in a clear sky), the sun visibility factor was 1, *average* brightness of the sky (measured over 30×30 portions of the image, as the average $((R + G + B)/3)$) was about 1.5 times the average brightness of the ground. Hence the polyhedral model evaluates to $(4 \times 1.5 \times g + g \times 1) = 7g$, meaning that the effect of ground reflection is $\frac{1}{7}$ of the effect of the skylight. Therefore, the linear shift is $\frac{1}{7}$ of the way between the color of the sky and the color of the ground. Using this method, the color of the incident light is estimated to be [0.284, 0.306]; as mentioned before, the observed color of the incident light (from the surface oriented vertically) was

[0.288, 0.302]. The previous section showed that the effect of ambient skylight accounted for a shift of 0.08 along the CIE linear function, from [0.180, 0.303] to [0.260, 0.299], which was about 74% of the total discrepancy of 0.108. The effect of ground light accounts for a shift of 0.025 along the CIE linear function, which is about 23% of the total discrepancy. Therefore, the combined effects of ambient skylight and ground reflection—under this set of conditions—account for about 97% of the discrepancy between the CIE model and our observations.

Since ground reflectance affects the color of the incident light, the albedo of the ground must be taken into account. The data collectd in this study was on two types of ground surface: concrete and (dead) winter grass. The average (again, over a 30×30 region) colors of the two types of ground were very similar, with both being the color of the incident light in the direction of the sun (see Fig. 4c). Hence, a "gray-world" assumption for the ground was reasonable in our data, but may not be reasonable for all types of ground cover. For instance, if images are taken in a field with bright green grass, the color of the ground reflection may be different. Another advantage of the polyhedral box model of the world is that it can accommodate the effect of miscellaneous scene objects on the color of the incident light, if their albedos and sizes are known.[8]

Finally, Fig. 4d shows seven samples of the white surface as its orientation changes from horizontal facing down to almost[9] horizontal facing up. The data shows that the measured color of the surface (i.e., the color of the effective incident light) is one of three colors: (a) the color of the sunlight (when the surface faces the ground, so that only reflected sunlight is incident upon it), (b) the combination of skylight and sunlight (when the both skylight and ground reflection are incident), and (c) only skylight, when no ground reflection is incident. This means that even if a surface is not exactly vertical, its effective incident light is the same combination of ambient skylight and ground reflection for a wide range of angles (along the elevation), as long as both sources are in the field-of-view of the surface.

For the samples of the clear sky with sun at 30°, the ground color was [0.372, 0.335]. Applying the polyhedral box model of daylight, the estimated linear shift due to ground reflection is about 0.013, which is about 19% of the total discrepancy (which, as shown earlier, was 0.69). For the overcast sky, there was no statistically significant discrepancy between the CIE model and our data. In the previous section, it was shown that the color of the ambient skylight under those conditions was uniform. Since the sun was completely occluded by clouds, the ground reflection was the color of the ambient light—[0.358, 0.335]. The sun visibility factor was 0; hence the polyhedral model of daylight predicts no shift from the average color of the sky.

3.3.3. Incident Light in the Direction of the Sun

The color of the incident light in the direction of the sun is not affected by ambient skylight or ground reflectance. When the white surface is sampled at various orientations between vertical and horizontal (facing the sky), the rgb color of the surface is unchanged. The reason the color of the incident sunlight is not "diluted" is that sunlight is significantly brighter than ambient skylight. Consequently, the effect of ambient skylight is negligible. This hypothesis is also supported by the fact that only about 1% of the CIE samples have an r value greater than the samples observed in our study.

[8] For instance, Gershon's approach [21] can take advantage of this model.

[9] Again, the surface is *almost* horizontal so that there is no sunlight incident upon it.

4. NORMALIZED SURFACE REFLECTANCE

The second model this paper proposes is a reflectance model to predict the color of the reflected light given the color of the incident light. We should emphasize our model is best described as a simplification of existing models. Several reflectance models exist, most notably Shafer's dichromatic model [50], Nayar *et al.*'s hybrid reflectance model [37], and Phong's shading model [45], all of which model surface reflectance as a linear combination of diffuse and specular reflection. These models, however, are more general than we need. Since we cannot predict the intensity of the incident daylight, only its normalized color, we only need to determine the normalized color of the reflected light. To this end, we derive the normalized photometric function, which is a simpler, normalized form of the dichromatic model.

4.1. Previous Physics-Based Models

The dichromatic reflectance model [50] represents the intensity of reflectance at wavelength λ for a surface at incident angle i, viewing angle e, and phase angle g as

$$L(\lambda, i, e, g) = m_s(i, e, g)c_s(\lambda) + m_b(i, e, g)c_b(\lambda), \tag{4}$$

where $c_s(\lambda)$ and $c_b(\lambda)$ are the albedos at wavelength λ for the specular and Lambertian components, respectively. c_s and c_b are surface properties and are dependent only on wavelength—not the illumination or viewing angles. The illumination and viewing angles determine the geometric scale factors $m_s(i, e, g)$ and $m_b(i, e, g)$, such that $(0 \leq m_s, m_b \leq 1)$. The dichromatic model shows that most of the (i, e, g) combinations will result in reflectance that is dominated by the Lambertian component; i.e., $m_s = 0$, $m_b = 1$. For the remaining angles, depending on the specularity of the surface, $0 \leq m_s, m_b \leq 1$. The points from each of the two components are represented as two linear clusters in a spectral histogram, which together form a skewed "$\perp$" along a dichromatic plane in *RGB* space.

According to the Phong shading model [45] (adapted for computer vision by Horn [27]), the brightness of reflectance (L) at incidence angle i, viewing angle e, and relative viewing angle n (which is the angle between the directions of viewing and maximal specular reflection) is

$$L(i, e, n) = t\frac{n+1}{2}\cos^{\alpha}(n) + (1-t)\cos(i), \tag{5}$$

where t and α are parameters of the material; t represents the total amount of light reflected by the specular component, and α represents the clustering of reflection of the specular component about the angle of reflection. In this model the falloff in the brightness of specular reflection is a function of $\cos^{\alpha}(n)$, and the weights for the two components are t and $(1-t)$. The value of α is determined empirically for a given surface and varies from 1 (for matte surfaces) to 200 (for highly specular surfaces). At $(\theta = 0)$, the brightness is maximal (i.e., 1), and falls off as the surface is rotated, to the minimum (i.e., 0) at -90° and 90°.

Finally, according to Nayar's hybrid reflectance model [37], the total intensity I at a given point in the surface is modeled by

$$I = A\cos(\theta_s - \theta_n) + B\delta(\theta_s - 2\theta_n), \tag{6}$$

where A and B are the weights of the Lambertian and specular components, respectively, and θ_s and θ_n are the angle of incidence and the direction of the surface normal.

The three models have characteristics in common:

- They model reflectance as a weighted linear combination of the Lambertian and specular components.
- The Lambertian component (also called "body reflection") is modeled according to Lambert's law [26].
- All three models predict intensity as a function of wavelength, which can then be represented in *RGB* as the brightness along each of the three dimensions.

There are also notable differences between the models:

- The Phong model assumes that the weights of the two components are dependent (t and $(1-t)$). Shafer and nayar do not explicitly assume dependency between the coefficients of the two components.
- The falloff models for the specular component are different: Nayar uses the delta function [38], Phong uses $\cos^{\alpha} n$, and Shafer does not specify a specular falloff function.
- Phong and Nayar, unlike Shafer, develop photometric functions that map from viewing and illuminant angles to reflectance.

Fortunately, the difference between these models are less important than their similarities for predicting normalized color. Since all three model reflectance as a linear combination of diffuse and specular reflection, there is very little difference between them in normalized rgb. This allows us to produce a simple, normalized reflectance model that can be easily fit to a small amount of data, but which is nonetheless consistent with the physical models above. In Appendix B this model is derived as a special case of Shafer's dichromatic model. It can also be derived from Phong's model, with the only difference being the rate of specular falloff.

4.2. The Normalized Reflectance Model

Unlike the models above, the normalized reflectance model predicts reflected colors in normalized rgb space. Because rgb is the result of normalizing the tristimulus *RGB* values by intensity, it is a two-dimensional space. The color of the illuminant is a point in normalized color space, and the color of a surface's diffuse reflection under that illuminant is another point. Since reflectance is modeled as a weighted combination of diffuse and specular components, all reflected colors lie on the line between these two points (as shown in Fig. 10). We call this line the normalized dichromatic line; it is the rgb equivalent of an observation by Lee *et al.* [33], who showed that the reflectances of surfaces form straight lines which converge at the color of the illuminant in CIE chromaticity space.

There are two parts to the normalized model of a surface. The first is the albedo of the surface, expressed as a 3×3 matrix M. This matrix maps the color of the illuminant to the color of the surface's diffuse reflection. The second is a photometric function that maps relative viewing angles onto positions on the normalized dichromatic line. Graphically, the photometric function can be displayed as in Fig. 6. The horizontal axis of the photometric function represents the relative viewing angle, which ranges from -90° to 90°. At $n = 0^{\circ}$, the viewing angle equals the angle of maximal specularity. The vertical axis ρ, scaled from 0 to 1, represents the relative distance between the color of the illuminant and the measured color of the diffuse reflectance under that illuminant.

To apply the normalized photometric function on a sunny day (when the sun visibility factor is 1), the color of the illuminant is estimated from Table 1. The measured color of the diffuse reflection is estimated by applying the color-coefficient matrix to the illuminant

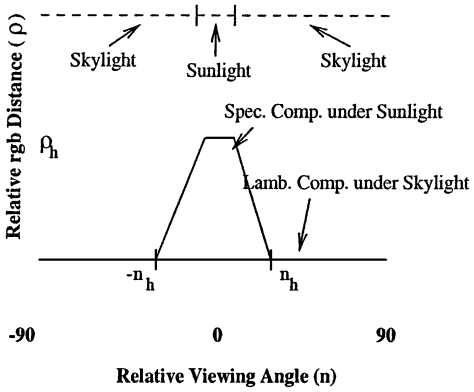

FIG. 6. The normalized photometric function for a surface with both diffuse and specular reflectance. The horizontal axis represents the relative viewing angle, while the vertical axis represents ρ, the position of the reflected color along the line between the color of the diffuse reflection under the illuminant and the color of the illuminant.

color. For every pixel, the relative viewing angle between the camera, surface, and illuminant is determined and converted to ρ through the photometric function. Since ρ determines the relative strengths of the diffuse and specular components of a surface, the measured color of the surface is $(1 - \rho)D + \rho I$, where D is the color of the diffuse reflection and I is the color of the illuminant. If the sun visibility factor is less than one, the value of ρ is multiplied by the sun visibility factor to prevent the sun from creating specular reflections on completely overcast days and to lessen the specular effect when the sun is partly obscured.

Since the color of the diffuse reflection D is MI, where M is the 3×3 albedo matrix and I is the color of the illuminant, the measured color of a surface according to the photometric function is

$$(1 - V\rho)IM + V\rho I, \tag{7}$$

where V is the sun visibility factor.

4.3. Fitting the Photometric Function

In the context of this work, we are interested in photometric functions that can be easily fit to a broad range of surfaces. It should be noted that detailed and highly accurate bidirectional reflectance distribution functions (BDRFs) have been fit to a library of materials [8], and that when applicable these more detailed models should be used in lieu of the comparatively crude photometric functions developed here. However, BDRFs are expensive to obtain[10] and may be unique to a surface if the surface has been painted or dyed or has weathered. Thus we present a cruder photometric model that can be fit to surfaces on just three loosely controlled outdoor images.

Looking back to Fig. 6, the peak of the photometric function under daylight is always a plateau, the width of which is the angle subtended by the sun. When viewed from earth, the sun subtends an angle of about 0.5° [56]. Hence the normalized photometric functions for all surfaces with both specular and diffuse components have a peak apex width of 0.5°. On either side of the peak there are falloff regions, where the specular reflection drops with

[10] The BDRFs in [8] were based on 205 carefully controlled laboratory images of each surface.

changes in the relative viewing angle. Outside of the falloff regions are base regions, where $\rho = 0$, implying that the surface exhibits no specular reflection at these viewing angles.

There are only two free parameters for the photometric function: the height of the peak, and the width of the base of the peak (which determines the slope of the falloff regions). The height of the peak determines the relative strengths of the specular and diffuse reflection when the relative viewing angle is zero. At this viewing angle, a shiny surface may reflect only the color of the illuminant, creating a peak of height one. Alternatively, a matte surface never exhibits a specular reflection, so the height of its peak is zero. Many objects are somewhere in the middle; when the relative viewing angle is zero, the surface reflects mostly the color of the illuminant, although some diffuse reflectance is mixed in. The result is a peak height between zero and one.

The width of the base of the specular peak determines the rate of specular falloff with respect to relative viewing angle. For smooth, specular surfaces, the percent of specular reflection drops off quickly as the magnitude of the relative viewing angle increases, creating a peak that is approximately the same width at its base as its apex, 0.5°. Rougher surfaces will still show some specular reflection at wider viewing angles, creating peaks that are broader at their base. For example, the width of the peak base for an imperfectly smooth surface such as a traffic sign is 4.5°; for shiny plastic surfaces, which are rougher, the width is about 7.2°.

In many respects, the width of the peak base is similar to the α parameter in the Phong model, except that the normalized photometric function assumes a linear dropoff while Phong models the rate of dropoff as the cosine of the relative viewing angle to the α power. Because the normalized photometric function uses a linear mode, it can be inferred from fewer samples. At the same time, we note that the rate of dropoff for most strongly specular surfaces is fast enough, relative to the uncertainty in the viewing angle, that the difference between the dropoff models may not be significant.

Figure 7 shows the photometric functions for five surfaces: matte paper, two traffic signs ("Stop" and "No Parking"), concrete, and asphalt. The functions for each surface were determined from just three images. The first image had a relative viewing angle of 0° at the center of the surface. Depending on the size of the surface, it subtends a range of viewing angles from -5° to 5° for the smallest surface up to -10° to 10° for the largest. The normalized photometric function was determined by selecting a row of pixels passing through the center of the surface and measuring the rgb values. This data was plotted as a two-dimensional function, with the relative viewing angle on the horizontal axis and the position of the rgb pixel on the normalized dichromatic line as the vertical axis. To reduce the effect of pixel-level noise, the value at each pixel is taken as the average over a 3×3 neighborhood. The other two images were used to sample reflectance outside of the $\pm 10^\circ$ viewing angle.

Photometric functions are then fit to this data according to one of two models. If a surface is matte and has no specular component, its photometric function is a straight line at $\rho = 0$. (The same is true for perfect mirrors that have no diffuse reflectance component, except that $\rho = 1$.) This is determined by fitting a straight line to the data points. If the resulting error is not statistically significant (according to the developed Gaussian noise model [5]), the fitted straight line serves as the photometric function for the surface. Otherwise, a single straight line at $\rho = 0$ is fitted to points in the range $-90^\circ \geq \theta \geq -n_h$, and a second straight line is fitted to the two points at $\theta = n_h$ and $\theta = 0.5^\circ$. Then, if this set of two lines can be symmetrically fit across the $\theta = 0^\circ$ axis to the remaining points, the symmetric piecewise linear function defines the photometric function for the surface.

Matte paper

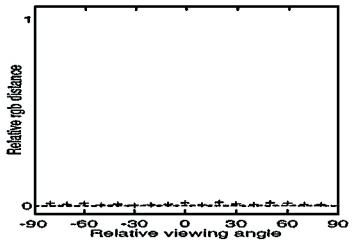

Concrete slab

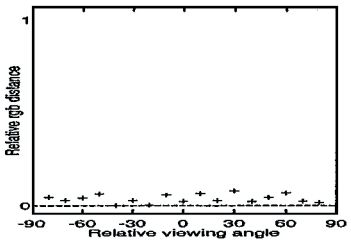

Road asphalt

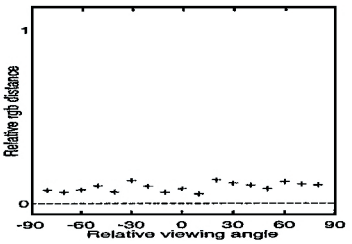

“No Parking” sign

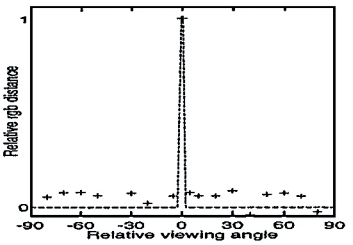

“Stop” sign

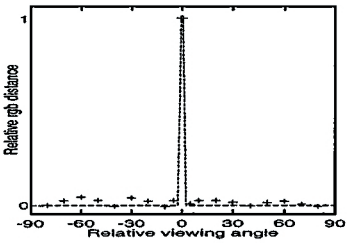

4-Color Artwork

FIG. 7. The normalized photometric functions for five surfaces.

Using this process, photometric functions were fit to five surfaces (matte paper, "Stop" sign, "No Parking" sign, concrete, and road asphalt), as shown in Fig. 7. For each surface, the function was fit to 17 points at various relative viewing angles. The average RMS errors between the data and the estimated functions were 0.007, 0.013, 0.081, 0.108, and 0.113, respectively. The errors are greater for the concrete, asphalt, and "No Parking" signs than for the other two surfaces because they have neutral colors (gray or white). As a result, their diffuse reflections are very close to the color of the illuminant, and even small errors in rgb appear magnified relative to the (very short) normalized dichromatic line.

5. ESTIMATING SURFACE COLOR

As stated in Section 1, one possible reason for developing models of illumination and reflectance is to predict the measured color of surfaces in outdoor images. This section tests the accuracy and precision of our models by applying them to 90 outdoor images of surfaces.

For these experiments, the measured color of a surface at a pixel was predicted by the following steps. Note that a Gaussian noise model is developed to account for experimental error [5]. Based on the noise model and corresponding receiver–operator characteristic (ROC) analysis [5], those pixels within 2σ of the estimate were classified as target, and all others as background. Hence, the accuracy of estimates is measured by the number of observed samples found to be within a 2σ confidence interval of the estimate. In addition, the precision of the estimate is measured by the area (in rgb space) of the 2σ confidence interval; in other words, the smaller the area of the interval, the tighter—i.e., more precise—the prediction.

The experimental steps are:

1. Predict the illuminant color: Look up the illumination color in Table 1, based on the sun angle, cloud cover, sun visibility, and whether the surface is pointed toward or away from the sun.
2. Find the normalized dichromatic line: One endpoint of the normalized dichromatic line is the color of the illuminant, as estimated in the previous step. The other is the result of multiplying the surface's albedo matrix with the color vector for the illuminant.
3. Compute the relative viewing angles: According to the standard pinhole camera model, the viewing ray extends from the focal point through a pixel to the surface. This ray is reflected around the surface normal to calculate the direction of reflection, and the relative viewing angle is the angle between the reflection ray and the ray from the illuminant (the sun) to the surface. Note that the relative viewing angle is slightly different for every pixel.
4. Predict color: Given the relative viewing angle for a pixel, the normalized photometric function (multiplied by the sun visibility factor) gives the position along the color line of the surface's measured color at that image position.

To further test the applicability of the models and the color prediction methodology, a series of pixel classification tests were conducted, in which image pixels were classified as either target or background. Such a classification provides two more performance measures: the true positive and false positive rates. The true positive rate is the percentage of on-target pixels that are correctly classified, while the false positive rate is the percentage of background pixels that are misclassified as target. As mentioned earlier, the classification assumes a 2σ confidence interval based on the derived Gaussian noise model and

corresponding ROC analysis [5]. For further details on the classification process, the reader is encouraged to consult the longer account of this study [5].

5.1. Case Studies of Surfaces

Images of the same five surfaces (matte paper, two traffic signs, and slabs of concrete and asphalt) were tested at four sun angles: 10°, 35°, 50°, and 60°; illumination and viewing angles were in the 0–180° and 0–80° rangs (in the azimuth), respectively. The cloud cover varied between 0 and 80%, with the sun visibility factor also varying between 0 and 1. The tests are grouped according to performance into two categories: the results for the matte paper, "No Parking" sign, and "Stop" sign were highly accurate, while those for the concrete and asphalt slabs were less so. Figure 8 shows representative prediction and classification results.

For the matte paper, tests were conducted on 20 images. Since the surface does not have a specular component, the prediction for all four conditions was a Gaussian distribution centered on a point in rgb space, which is the color of the diffuse reflection under the predicted illuminant. For each of the 20 images, the observed color of the surface was determined by averaging a 20×20 region of the image. All 20 observed colors were within the 2σ confidence interval of the estimates under the corresponding conditions. On average, the estimated rgb was 0.005 away from the observed rgb. In the pixel classification tests—represented by Fig. 8a—the true positive rate was 96.3%, with a false positive rate of 1.2%. One reason for the accuracy of the estimate is that the surface is matte, virtually eliminating errors due to the photometric function and viewing angle. In effect, this data simply confirms that our illumination model is reasonably accurate.

For the "No Parking" sign, the white portion of the surface is considered the target, while the red lettering is considered part of the background. The "No Parking" sign was tested under five sets of conditions. Because the surface is specular, three types of predictions are possible: (a) pure Lambertian reflections distributed around a single rgb point, which occur at large relative viewing angles or when the sun is not visible; (b) pure specular reflections, which are also distributed around a single rgb point and occur at relative viewing angles less than 0.5°; and (c) mixed reflections, occurring at relative angles between these two extremes and distributed along the normalized dichromatic line. In the first two cases, estimates of the colors are sampled over the largest possible uniformly colored surface region in the image.[11] However, the portion of the image representing the transition pixels is not uniformly colored; hence individual pixels are extracted, each representing a different rgb color. In the purely diffuse case, all 19 observations were within the 2σ confidence interval of the estimates under the corresponding conditions; the average error between the estimated and observed rgb colors was about 0.004, and the area of the confidence interval was about 0.0003. For the pure specular cases all 12 were within the confidence interval, with an average error of 0.006; the area within the confidence interval was about 0.0003. For the transition cases 11 out of the 12 samples were with the confidence interval, with an average error (measured as the perpendicular distance to the estimated dichromatic line segment) of 0.011. The area of the ellipse representing the confidence interval was about 0.0006 square units, or twice the size of the prediction in the purely diffuse case. As with the matte paper, the errors for the "No Parking" sign are small, and all but one of the observed values are within the

[11] Typically, this region is smaller than the 20×20 regions used for the matte surface.

4-Color Artwork

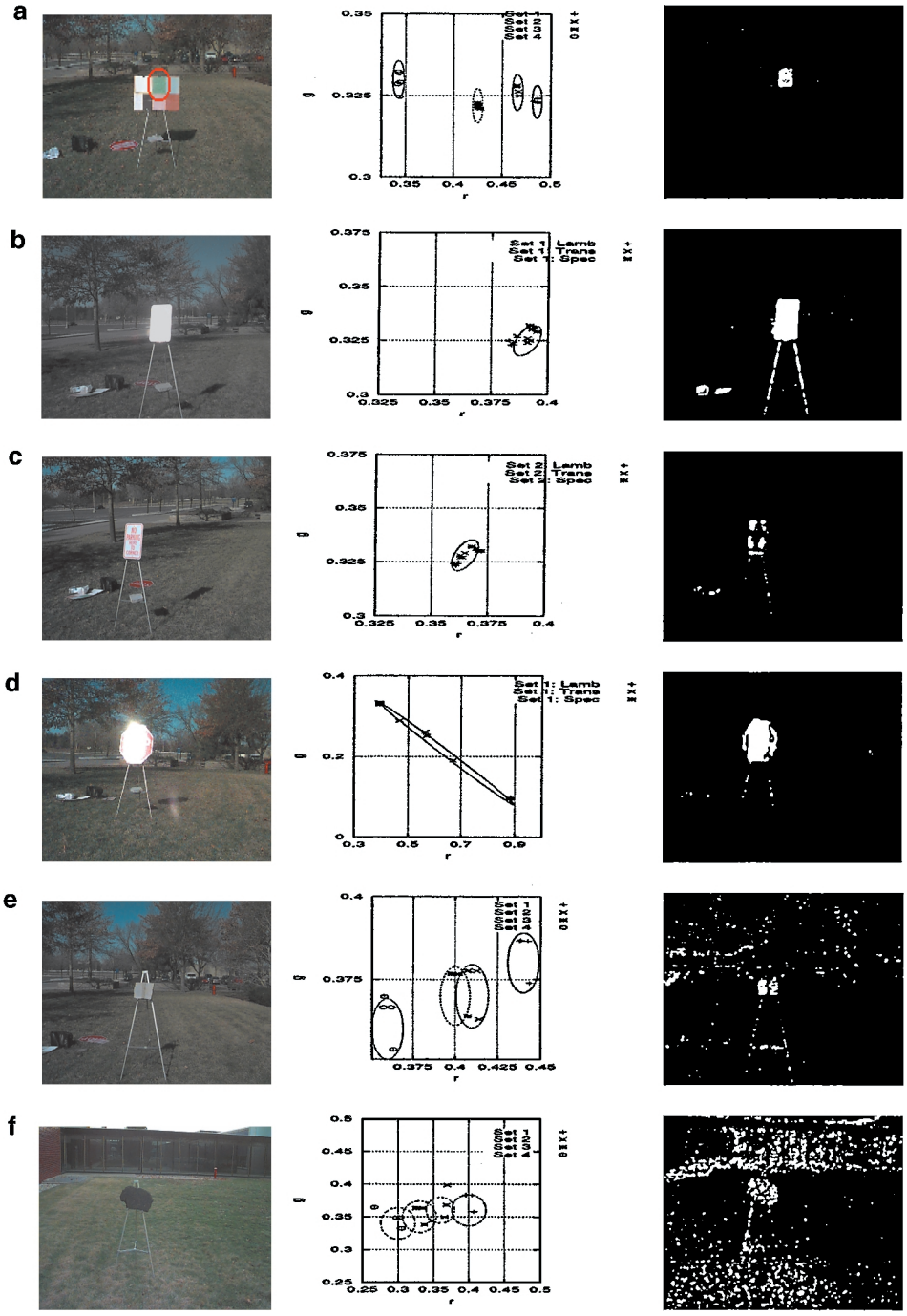

FIG. 8. Surface color prediction and subsequent pixel classification: (a) Matte paper, true positives: 96.3%; false positives: 1.2%. (b) "No Parking" sign, specular case, true positives: 91.2%; false positives: 3.6%. (c) "No Parking" sign, non-specular case, true positives: 95.8%; false positives: 4.4%. (d) "Stop" sign, true positives: 97.1%; false positives: 5.1%. (e) Concrete slab, true positives: 75.9%; false positives: 12.1%. (f) Road asphalt, true positives: 61.8%; false positives: 20.8%.

confidence interval of the estimate. The "No Parking" sign is specular; hence, errors due to the photometric function and relative viewing angle are included. However, because the albedo of the surface is neutral (near-white), the color of its Lambertian component is very close to the color of its specular component. Hence, the dichromatic line is very short, and errors due to the relative viewing angle and/or the photometric function have only a small impact. Because of specular reflection, almost of the entire surface of the sign, including the lettering, is the color of the illuminant. Hence, the target color is the color of the illuminant, which includes pixels from all surfaces exhibiting a specular reflection, as well as pixels on surfaces with neutral colors (whites and grays). The respective average true positive and false positive rates for the "No Parking" sign were 97.1 and 5.1% for the specular cases; for the nonspecular cases, the true positive and false positive rates were 91.2 and 3.6%, respectively; Figs. 8b and 8c show representative results. The results also show small clusters of pixels from background objects (such as the concrete slab under the easel) that are classified as target pixels. These objects have neutral albedos and hence also reflect the color of the illuminant.

Another issue with the "No Parking" sign (and the "Stop" sign, to be discussed shortly) is that of mixed pixels, which are pixels on or near the edge between the lettering and the body of the sign. Due to pixel interpolation, these pixels are neither the "white" of the sign nor the "red" of the lettering, but a mixture of the two. These pixels are not considered targets and would result in larger errors if they were. To identify mixed pixels and eliminate them from consideration, it was assumed that the mixed pixels form a line between the pixels on the (white) target area and the (red) lettering. Such a hypothetical line was estimated for the target and lettering pixels in the Lambertian viewing range.[12] All pixels within the 2σ confidence interval of this line were considered mixed pixels and were eliminated from consideration during evalution. Figure 8c shows that only about half of the actual sign is classified as target. Specifically, there are two portions of the "No Parking" sign that are classified as background: the lettering and the pixels in the immediate neighborhood of the lettering. The lettering really is background and should be classified as such. However, the pixels neighboring the lettering are polluted by the mixed-pixel effect. Because of pixel interpolation, the color of mixed pixels is somewhere between the color of the lettering and that of the target area. The mixed pixels were not considered part of the target; if they were, the true positive rate would drop to about 83.4% for the nonspecular conditions. Even without the specular effect, the albedo of the "No Parking" sign is almost neutral (i.e., white). As with the previous example, some pixels from background concrete and other neutral colored objects are classified as targets.[13]

For the "Stop" sign, the red portion of the surface is considered the target area, and the white lettering and border is considered background. As with the "No Parking" sign, three types of reflection occur: pure diffuse, pure specular, and combined "transition" reflection. For the diffuse cases, all 19 estimates were within the 2σ confidence interval, with an average error of 0.005; the area of the confidence interval was 0.0004 square units. For the pure specular cases, all 12 observed values were within the interval of the prediction, with an average error of 0.006; the area of the confidence interval was 0.0005. For the

[12] Note that the specular range was not used because the target and lettering areas are both specular and would look identical under specular conditions.

[13] Note that specular reflection can often cause pixel saturation in images. In our case, the camera f-stop adjustment prevented pixel saturation in most cases.

transition cases, 9 out of the 12 samples were within the interval, with an average error of 0.017, and a confidence interval of area 0.001 square units. One reason for the higher errors from the transition pixels is the mixed pixel effect, caused due to their proximity to pixels from the diffuse and specular cases. In the pixel classification tests for the "Stop" sign, the average true positive rate was 95.8%; the average false positive rate was 4.4% (see Fig. 8d).

While the results for the matte surface, "No Parking" sign, and "Stop" sign were quite accurate, tests on the concrete and asphalt surfaces were less so. For the concrete surface, tests were conducted on 16 images under four conditions. The concrete slab is not uniformly colored, as a consequence of which the standard deviation of the rgb colors over the surface is 0.009, significantly higher than for the matte surface or the Lambertian samples of the traffic signs. This has two consequences: first, the prediction is less precise, in that the area within the confidence interval is large; second, samples not included in the original estimate of the standard deviation can be outside the confidence interval. Out of 16 observed values, 14 were within the 2σ confidence interval of the corresponding estimates. The average error between estimated and observed values was about 0.011. The area within the interval averaged about 0.001 square units. The average true positive pixel classification rate for the concrete slab was 75.9%, with a 12.1% false positive rate (see Fig. 8e). Note that the vertical strip in the middle of the asphalt is slightly off color, explaining the region in the middle classified as nontarget. The concrete slab was chosen for its neutral "grayish" color, and the number of false positives is due mostly to the presence of several other surfaces of neutral color. As in the case of the traffic signs under the specular effect, color neutrality makes detection difficult because there are likely to be several neutrally-colored surfaces in a typical outdoor scene (such as concrete, pavement, road, etc., and surfaces exhibiting specular reflection). The examples of the traffic signs and the concrete surface illustrate another phenomenon common to neutral-colored surfaces and to surfaces with strong specular components. This effect can be understood by imagining the rgb normalized dichromatic lines for a number of surfaces, some specular and some neutral-colored. All these lines coincide at the illuminant point, making that part of the color space ambiguous for recognition. Pixels that are the color of the illuminant can belong to any specular or neutral-colored surface in the scene. Lee *et al.* [33] describe a number of examples of such surfaces, along with their reflectances in normalized color space.

The results from the slab of road asphalt (Fig. 8f) were worse than those for the concrete slab—the average error between the estimated and observed rgb values was 0.011, and only 13 of the 16 samples were within the confidence interval. The reason for the poor performance is a more extreme case of what affected the concrete slab: the road surface is of neutral—although not uniform—color. It has a standard deviation of 0.012, and the confidence interval of the predicted color has an area of about 0.002 square units. For the asphalt slab, the true positive classification rate was 61.8%, and the false positive rate was 20.8%. The examples of the road surface and the concrete slab show that for neutral colors, there is so little color information that color may not be a good feature for recognition.

6. CONCLUSIONS

This paper demonstrates the disadvantages of using the CIE model for predicting color in outdoor images. As a solution, it develops a model of daylight that is more appropriate for outdoor machine vision applications, in that it (i) is indexed by imaging conditions and

(ii) simulates a wide field of view. This makes it possible to predict the color of light incident on flat surfaces in outdoor scenes. There are, however, some limitations to this model. The robustness of the model across a broad range of tests is yet to be proven. In particular, the date for the daylight model was sampled at three relatively similar geographical locations in North America; it is not clear if it applies to other parts of the world. Specifically, the effect of humidity, haze, and other particulate matter in the air may significantly affect the model. In addition, the daylight model does not account for the effect of light reflected from objects other than the ground. Nonetheless, it provides a method for approximating the color of daylight in real images.

This paper also presents a reflectance model for surfaces with combined diffuse and specular reflection in normalized rgb color space. This model is consistent with previous physics-based models, and yet is simpler to use when predicting normalized reflectance.

Experimentally, this paper shows that the illumination and reflectance models developed here can classify pixels based on a 2σ confidence interval around their predicted color. For surfaces with nonneutral colors, this classification had a true positive rate in the mid-90s for most viewing and illumination conditions, with false negative rates generally at or under 5%. Even for neutral-colored objects, we are able to identify target pixels around 70% of the time, with false negative rates (on average) of less than 20%. The tests with neutral-colored objects do show two weaknesses of this approach in unconstrained applications: first, there may not be enough color information for recognizing neutral-colored surfaces in normalized color space; second, surfaces that are not uniformly colored cannot be easily modeled using such a method.

7. APPENDIX A: CAMERA RESPONSE PARAMETERS

Table 2 describes the response parameters of the camera used in this study. We did not test the robustness of the empirical methods across multiple cameras and assume that calibration of specific cameras against the parameters in Table 2 will not adversely affect performance. Figure 9 depicts the geometry of illumination and viewing.

Au: Figure 9 call-out ok?

TABLE 2
Parameters of the Camera Used in This Study

Factor	Model	Comments
Focal length	6.5 mm (equivalent to 37 mm on a 35 mm camera)	
Color filters	Based on NTSC RGB standard primaries [47]	Calibration required
White point	0.326, 0.341, 0.333	Obtained with a calibrated white surface (Munsell $N9/$) under D65 illuminant
Gamma correction	$\gamma = 0.45$	f-stop adjusted to stay in the 50–75%, approximately linear output range
Aperture range	$f/2.8$ to $f/16$	Aperture adjusted with f-stop
Shutter speed	1/30 to 1/175 s	
Image resolution	756×504, 24-bit RGB	
Gain	2.0 e-/count	Fixed

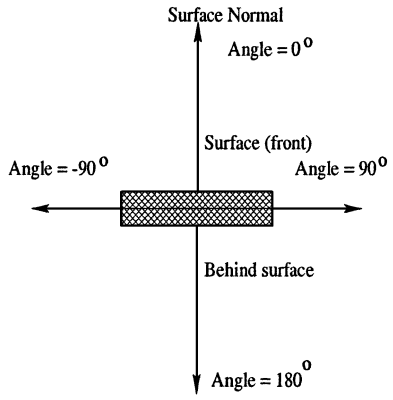

FIG. 9. The geometry of illumination and viewing depends on the position of the illuminant and camera (respectively) with respect to the surface. Along the surface normal, the angle 0°, and ranges from −90° to 90°. The *relative viewing geometry* is the combination of the illumination and viewing geometries.

8. APPENDIX B: DERIVATION OF THE NORMALIZED REFLECTANCE MODEL

The normalized reflectance model predicts the reflected color of daylight from the color of the illuminant light plus scene geometry. It has two components: a nine-parameter model of surface albedo and a two-parameter normalized photometric function. This appendix derives the normalized reflectance model as a special case from Shafer's dichromatic model, as given by the equation below.

$$L(\lambda, i, e, g) = m_s(i, e, g)c_s(\lambda) + m_b(i, e, g)c_b(\lambda). \tag{8}$$

The first step toward simplifying Eq. (8) is to note that with the exception of a few surface types (such as fluorescent paints and certain metals [22]), specular surfaces reflect back the color of the illuminant, with a uniform albedo; hence, $c_s(\lambda) = 1$.

The second simplification links the specular and diffuse constants. In the dichromatic model, the condition $0 \leq m_s,\ m_b \leq 1$ is true, but the condition $m_s + m_b = 1$ is not. However, in normalized rgb, $m_s + m_b = 1$ is always true[14] by virtue of the color space being normalized. In particular, according to the weighted-combination reflectance models $R_a = W_l R_l + W_s R_s$, $G_a = W_l G_l + W_s G_s$, and $B_a = W_l B_l + W_s B_s$, where R_a, G_a, and B_a are the measured colors of the surface, R_l is the albedo of the red component, W_l the weight of the Lambertian component, and so on. In rgb, $r = \frac{R}{R+G+B}$. Hence, $r_a = W_l(\frac{R_l}{R_l+G_l+B_l}) + W_s(\frac{R_s}{R_s+G_s+B_s})$. If the two weighted are multiplied by any constant A (representing intensity), then the values of R, G, and B are all multiplied by A, leaving the normalized r, g, b values unchanged. Hence, we can scale the weights to sum to any constant; we choose $W_l + W_s = 1$.

Therefore, in rgb the dichromatic model can be simplified to

$$L(\lambda, i, e, g) = (1 - m_b(i, e, g)) + m_b(i, e, g)c_b(\lambda).$$

The dichromatic model uses the phase angle g, in addition to the incidence angle i and

[14] Note that this assumption is also made in the models derived by Phong [45] and Horn [27].

the viewing angle e. According to the Lambertian model [26], brightness—not normalized color—is a function of the phase angle. Hence, g can be simplified as the sum of i and e. Finally, by expressing the combination of i and e as the relative viewing angle n, i.e., the difference between the viewing angle and the angle of maximal specularity (as in the Phong model), the dichromatic model can be reduced to

$$L(\lambda, n) = (1 - m_b(n)) + m_b(n)c_b(\lambda). \tag{9}$$

In Eq. (9) the Lambertian component is defined in terms of wavelength. According to the Lambertian model, the energy reflected at a given wavelength λ is measured as the product of the incident light and the surface albedo [26]

$$\rho(\lambda) = \iota(\lambda)\cos(\theta_i)\sigma(\lambda), \tag{10}$$

where $\rho(\lambda)$ and $\iota(\lambda)$ denote the intensity of the reflected and incident light at wavelength λ, respectively, θ_i is the angle of incidence, and $\sigma(\lambda)$ is the surface albedo for light at wavelength λ. In normalized color space, the brightness component of the Lambertian model is eliminated. Hence, the cosine factor in Eq. (10) is dropped

$$\rho(\lambda) = \iota(\lambda)\sigma(\lambda). \tag{11}$$

Equation (11) can be converted to rgb by using the (calibrated) response functions of the camera, and then normalizing over intensity, to get

$$\begin{aligned} r &= \int E(\lambda)\bar{r}(\lambda)\,\delta\lambda \\ g &= \int E(\lambda)\bar{g}(\lambda)\,\delta\lambda \\ b &= \int E(\lambda)\bar{b}(\lambda)\,\delta\lambda, \end{aligned} \tag{12}$$

where r, g, and b are the normalized color values derived by applying filters $\bar{r}$, $\bar{g}$, and $\bar{b}$ to the spectral power distribution of the incident light (E) at wavelength λ. Equation (12) shows a discrete, three-dimensional approximation of a continuous function in wavelength space. By applying this approximation to the model from Eq. (12), the Lambertian color-coefficient model is (see [44])

$$\begin{aligned} r &= r_i * W_{rr} + g_i * W_{rg} + b_i * W_{rb} \\ g &= r_i * W_{gr} + g_i * W_{gg} + b_i * W_{gb} \\ b &= r_i * W_{br} + g_i * W_{bg} + b_i * W_{bb}, \end{aligned} \tag{13}$$

where r_i, g_i, and b_i represent the color of the incident light, and W_{rr}, W_{rg}, and W_{rb} are the color coefficients (albedo) of the red component of the surface under the red, green, and blue bands of the illuminant, respectively; the expressions associated with g and b are analogous. According to this model, the measured color of the diffuse reflection component constitutes a linear transform of the incident light, the coefficients of which are determined by the spectral reflectance of the surface. The nine weights can be determined from a total

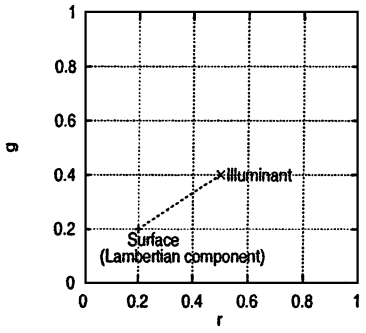

FIG. 10. The dichromatic reflectance model in normalized color space. The measured color of the surface is a point on the line between the points representing the colors of the illuminant and the Lambertian component of the surface under that illuminant.

of three images each under different illuminating conditions (the three images constitute a total of nine equations for determining the coefficients, three each of r, g, and b). Note that the off-diagonal terms in the matrix are non-zero due to the overlap in the tristimulus functions [22] (except in some restricted cases of illuminants and reflectances [12]). **Au: As meant?**

In matrix notation, the color-coefficient model is represented as

$$\begin{bmatrix} r \\ g \\ b \end{bmatrix} = \begin{bmatrix} W_{rr} & W_{rg} & W_{rb} \\ W_{gr} & W_{gg} & W_{gb} \\ W_{br} & W_{bg} & W_{bb} \end{bmatrix} \begin{bmatrix} r_i \\ g_i \\ b_i \end{bmatrix}. \tag{14}$$

Earlier, in Eq. (9), the Lambertian component was represented by $m_b(n)c_b(\lambda)$, which is the wavelength form of the color-coefficient model shown in Eq. (14), above. In normalized rgb, the diffuse reflection is a point in the rgb plane determined by applying the diffuse color-coefficient matrix to the normalized color of the illuminant. The specular component, represented in Eq. (9) as $(1 - m_b(n))$, is an offset from the diffuse reflection point in the direction of the illuminant color. Figure 10 shows this phenomenon.

This confirms that in rgb (as in RGB), surface reflectance can be modeled as a weighted combination of diffuse and specular reflection. In rgb, however, the two reflectance components are represented as points, rather than as two lines as in the dichromatic model; one of these points represents the illuminant, and the other represents the measured color of the Lambertian component under that illuminant. Note that the illuminant point also represents the measured color of the pure specular component, because under pure specular reflectance, the measured normalized color of the surface is that of the illuminant. This phenomenon was also observed by Lee *et al.* [33].

REFERENCES

1. T. E. Boult and G. Wolberg, Correcting chromatic aberrations using image warping, in *DARPA Image Understanding Workshop, 1992*.
2. G. Buchsbaum, A spatial processor model for object colour perception, *J. Franklin Inst.* **310**, 1980, 1–26.
3. W. Budde, Unpublished. Referenced in [29]. **Au: Pls. provide title of paper, sponsoring society, and date.**
4. S. Buluswar and B. Draper, Color recognition in outdoor images, in *Proceedings of the International Conference on Computer Vision, 1998*.

5. S. Buluswar, *Models for Outdoor Color Vision*, Doctoral dissertation, University of Massachusetts, Amherst, 2000.
6. H. R. Condit and F. Grum, Spectral energy distribution of daylight, *J. Opt. Soc. Amer.* **54**(7), 1964, 937–944.
7. J. Crisman and C. Thorpe, Color vision for road following, in *Vision and Navigation: The Carnegie Mellon NAVLAB*, Kluwer Academic, Dordrecht/Norwell, MA, 1990.
8. K. Dana, B. van Ginneken, S. Nayar, and J. Koenderink, Reflectance and texture of real world surfaces, *ACM Trans. Graph.* **18**(1), 1999, 1–34.
9. B. Draper, C. Brodley, and P. Utgoff, Goal-directed classification using linear machine decision trees, *IEEE Trans. Pattern Anal. Mach. Intell.* **16**(9), 1994, 888–893.
10. G. D. Finlayson, Color constancy in diagodiagonalnal chromaticity space, in *Proceedings of the Fifth International Conference on Computer Vision, 1995.*
11. G. D. Finlayson, B. V. Funt, and K. Barnard, Color constancy under varying illumination, in *Proceedings of the Fifth International Conference on Computer Vision, 1995*.
12. G. D. Finlayson, M. S. Drew, and B. V. Funt, Diagonal transforms suffice, *J. Opt. Soc. Amer.* **11**(11), 1994, 3011–3019.
13. G. D. Finlayson, S. D. Hordley, and P. M. Hubel, Color by correlation: A simple, unifying approach to color constancy, in *Proceedings of the International Conference on Computer Vision, 1998*.
14. D. Forsyth, A novel approach for color constancy, *Internat. J. Comput. Vision* **5**, 1990, 5–36.
15. W. Freeman and D. Brainard, "Bayesian Decision Theory: the maximum local mass estimate," *Proceedings of the Fifth International Conference on Computer Vision*, 1995.
16. B. V. Funt and G. D. Finlayson, "The State of Computational Color Constancy," *Proceedings of the First Pan-Chromatic Conference,* Inter-Society Color Council, 1995.
17. B. V. Funt and M. S. Drew, "Color Space Analysis of Mutual Illuminations," *IEEE Transactions on Pattern Analysis and Machine Intelligence* **12**, 1993, 1319–1326.
18. B. V. Funt and G. D. Finlayson, "Color constant color indexing" *IEEE Transactions on Pattern Analysis and Machine Intelligence* **17**(5), 1995, 522–529.
19. B. V. Funt, K. Barnard, and L. Martin, "Is Machine Color Constancy Good Enough?," *Proceedings of the Fifth European Conference on Computer Vision, 1998*.
20. B. V. Funt, V. C. Cardei, and K. Barnard, "Method of Estimating Chromaticity of Illumination using Neural Networks" *Proceedings of the IS&T/SID Fourth Color Imaging Conference, 1996*.
21. R. Gershon, A. Jepson, and J. Tsotsos, *The Effects of Ambient Illumination on the Structure of Shadows in Chromatic Images*, RBCV-TR-86-9, Department of Computer Science, University of Toronto, Toronto, Canada, 1986.
22. F. Grum and C. Bartleson, *Optical Radiation Measurements: Color Measurement*, Academic Press, San Diego, 1980.
23. S. T. Henderson and D. Hodgkiss, The spectral energy distribution of daylight, *British J. Appl. Phys.* **14**, 1963, 125–131.
24. R. Henry, Colorimetry in the natural atmosphere, in *Proceedings of the First Pan-Chromatic Conference, 1995*.
25. F. S. Hill, *Computer Graphics*, Macmillan Co., New York, 1990.
26. B. K. P. Horn, *Robot Vision*, MIT Press, Cambridge, MA, 1987.
27. B. K. P. Horn, Understanding image intensities, *Artific. Intell.* **8**, 1977, 201–231.
28. P. Horowitz and W. Hill, *The Art of Electronics*, Cambridge Univ. Press, Cambridge, UK, 1989.
29. D. Judd, D. MacAdam, and G. Wyszecki, Spectral distribution of typical daylight as a function of correlated color temperature, *J. Opt. Soc. Amer.* **54**(8), 1964, 1031–1040.
30. G. J. Klinker, S. A. Shafer, and T. Kanade, Color image analysis with an intrinsic reflection model, in *Proceedings of the International Conference on Computer Vision, 1988*.
31. J. von Kries, Die Gesichtsempfindungen, in *Handbuch Physiologie Menchen, 1904.* **Au: Pub.? city?**
32. E. H. Land, Lightness and retinex theory, *Scientif. Amer.* **237**(6), 1977, 108–129.
33. H. C. Lee, E. J. Breneman, and C. P. Schulte, Modeling light reflection for computer color vision, *IEEE Trans. Pattern Anal. Mach. Intell.* **12**, 1990, 402–409.

34. L. T. Maloney and B. A. Wandell, Color constancy: A method for recovering surface spectral reflectance, *J. Opt. Soc. Amer. A* **3**, 1986, 29–33.
35. B. A. Maxwell and S. A. Shafer, A framework for segmentation using physical models of image formation, in *IEEE Computer Society Conference on Computer Vision and Pattern Recognition, 1994*.
36. J. Meeus, *Astronomical Formulae for Calculators*, Willman-Bell, Richmond, 1985.
37. S. K. Nayar, K. Ikeuchi, and T. Kanade, Determining shape and reflectance of hybrid surfaces by photometric sampling, *IEEE Trans. Robot. Automat.* **6**, 1990, 418–431.
38. S. K. Nayar, K. Ikeuchi, and T. Kanade, Surface reflection: Physical and geometric perspectives, technical report, CMU-RI-TR-89-7, Carnegie Mellon University, Pittsburgh, 1989.
39. C. Novak, S. Shafer, and R. Wilson, Obtaining accurate color images for machine vision research, in *Proceedings of the SPIE, 1990*.
40. C. Novak and S. Shafer, *A method for Estimating Scene Parameters from Color Histograms*, technical report, CMU-CS-93-177, Carnegie Mellon University School of Computer Science, Pittsburgh, 1993.
41. Y. Ohta and Y. Hayashi, Recovery of illuminant and surface colors from images based on the CIE daylight, in *Proceedings of the Third European Conference on Computer Vision, 1994*.
42. Y. Ohta, *A Region-Oriented Image-Analysis System by Computer*, Doctoral dissertation, Kyoto University, Kyoto, Japan, 1980.
43. J. Parkkinen, Color spectra database, Lappeenranta University of Technology online data; *available at* http://www.lut.fi/ltkk/tite/research/color/lutcs_database.html.
44. A. Petrov, Surface color and color constancy, *J. Color Res. Appl.* **18**(4), 1993, 236–240.
45. B. T. Phong, Illumination for computer generated images, *Comm. Assoc. Comput. Mach.* **18**, 311–317. **Au: Year?**
46. D. A. Pomerleau, *Neural Network Perception for Mobile Robot Guidance*, Kluwer Academic, Boston, 1993.
47. D. Rogers, *Procedural Elements for Computer Graphics*, McGraw–Hill, New York, 1985.
48. Y. Sato and K. Ikeuchi, Reflectance analysis under solar illumination, in *Proceedings of the IEEE Workshop for Physics-Based Modeling in Computer Vision, 1995*.
49. B. J. Schachter, L. S. Davis, and A. Rosenfeld, Some experiments in image segmentation by clustering of local feature values, *Pattern Recognition* **11**(1), 1979, 19–28.
50. S. A. Shafer, Using color to separate reflection components, *Color Res. Appl.* **10**, 1985, 210–218.
51. J. L. Simonds, Application of characteristic vector analysis to photographic and optical response data, *J. Opt. Soc. Amer.* **53**(8), 1963.
52. M. J. Swain and D. H. Ballard, Color indexing, *Internat. J. Comput. Vision* **7**, 1991, 11–32.
53. M. J. Vrhel and H. J. Trussell, Filter considerations in color correction, *IEEE Trans. Image Process.* **3**, 1994, 147–161.
54. A. Yuille, A method for computing spectral reflectance, *Biolog. Cybernet.* **56**, 1987, 195–201.
55. M. D'Zmura and G. Iverson, Color constancy: Basic theory of two stage linear recovery of spectral descriptions for lights and surfaces, *J. Opt. Soc. Amer. A* **10**, 1993, 2148–2165.
56. M. Zombeck, *Handbook of Space Astronomy and Astrophysics*, Cambridge Univ. Press, Cambridge, UK, 1990.